

THE GRISM LENS-AMPLIFIED SURVEY FROM SPACE (GLASS). VIII. THE INFLUENCE OF THE CLUSTER PROPERTIES ON H α EMITTER GALAXIES AT $0.3 < z < 0.7$

BENEDETTA VULCANI¹, TOMMASO TREU², CARLO NIPOTI³, KASPER B. SCHMIDT⁴, ALAN DRESSLER⁵, TAKAHIRO MORSHITA^{2,6,7},
BIANCA M. POGGIANTI⁸, MATTHEW MALKAN², AUSTIN HOAG⁹, MARUSA BRADAČ⁹, LOUIS ABRAMSON², MICHELE TRENTI¹,
LAURA PENTERICCI¹⁰, ANJA VON DER LINDEN¹¹, GLENN MORRIS^{12,13}, AND XIN WANG²

¹School of Physics, University of Melbourne, VIC 3010, Australia

²Department of Physics and Astronomy, University of California, Los Angeles, CA, USA 90095-1547

³Department of Physics and Astronomy, Bologna University, viale Berti-Pichat 6/2, I-40127 Bologna, Italy

⁴Leibniz-Institut für Astrophysik Potsdam (AIP), An der Sternwarte 16, 14482 Potsdam, Germany

⁵The Observatories of the Carnegie Institution for Science, 813 Santa Barbara St., Pasadena, CA 91101, USA

⁶Astronomical Institute, Tohoku University, Aramaki, Aoba, Sendai 980-8578, Japan

⁷Institute for International Advanced Research and Education, Tohoku University, Aramaki, Aoba, Sendai 980-8578, Japan

⁸INAF-Astronomical Observatory of Padova, Italy

⁹Department of Physics, University of California, Davis, CA, 95616, USA

¹⁰INAF - Osservatorio Astronomico di Roma Via Frascati 33 - 00040 Monte Porzio Catone, I

¹¹Stony Brook University Department of Physics and Astronomy Stony Brook, NY 11794

¹²Kavli Institute for Particle Astrophysics and Cosmology, Stanford University, 452 Lomita Mall, Stanford, CA 94305-4085, USA and

¹³SLAC National Accelerator Laboratory, 2575 Sand Hill Road, Menlo Park, CA 94025, USA

Draft version July 12, 2018

ABSTRACT

Exploiting the data of the Grism Lens-Amplified Survey from Space (GLASS), we characterize the spatial distribution of star formation in 76 high star forming galaxies in 10 clusters at $0.3 < z < 0.7$. All these galaxies are likely restricted to first infall. In a companion paper we contrast the properties of field and cluster galaxies, whereas here we correlate the properties of H α emitters to a number of tracers of the cluster environment to investigate its role in driving galaxy transformations. H α emitters are found in the clusters out to 0.5 virial radii, the maximum radius covered by GLASS. The peak of the H α emission is offset with respect to the peak of the UV-continuum. We decompose this offsets into a radial and tangential component. The radial component points away from the cluster center in 60% of the cases, with 95% confidence. The decompositions agree with cosmological simulations, i.e. the H α emission offset correlates with galaxy velocity and ram-pressure stripping signatures. Trends between H α emitter properties and surface mass density distributions and X-ray emissions emerge only for unrelaxed clusters. The lack of strong correlations with the global environment does not allow us to identify a unique environmental effect originating from the cluster center. In contrast, correlations between H α morphology and local number density emerge. We conclude that local effects, uncorrelated to the cluster-centric radius, play a more important role in shaping galaxy properties.

Subject headings: galaxies: general – galaxies: formation – galaxies: evolution

1. INTRODUCTION

Galaxy properties have been found to strongly correlate with environment, at different redshifts (e.g. Butcher & Oemler 1984; Dressler 1980; Dressler *et al.* 1997; Poggianti *et al.* 1999; Ellis *et al.* 1997; Lewis *et al.* 2002; Treu *et al.* 2003; Gómez *et al.* 2003; Goto *et al.* 2003; Postman *et al.* 2005; Kauffmann *et al.* 2004; Grützbauch *et al.* 2011). One of the most striking differences between galaxies in clusters and in the field is the fraction of star forming galaxies, which decreases from the densest to the sparsest environments (e.g. von der Linden *et al.* 2010; Paccagnella *et al.* 2016). The evolution of the star formation activity is paralleled by a corresponding evolution of galaxy morphologies from late- to early-types, whose occurrence is environment-dependent (Dressler *et al.* 1997; Fasano *et al.* 2000; Capak *et al.* 2007; Poggianti *et al.* 2009; Oesch *et al.* 2010; Vulcani *et al.* 2011).

A central question in this picture is how much galaxy evolution is driven by internal processes as opposed to collective phenomena found only in specific environments. However, as pointed out by De Lucia & Borgani (2012), the distinction is not clear cut: today's clusters correspond to some of the most overdense regions in the early Universe and therefore we expect their evolution to be accelerated with respect to aver-

age or underdense region, even if cluster-specific mechanisms were not at all relevant (Dressler 1980; Abramson *et al.* 2016; Lilly & Carollo 2016; Morishita *et al.* 2016).

Several properties of dense galaxy clusters give rise to physical processes that have been suggested to transform the galaxy morphological and star-forming properties. For example, strong tidal effects can distort a galaxy and tear away stars and gas (Bekki 1999). Rapid, frequent galaxy-galaxy encounters induce gravitational perturbations which can greatly affect the stellar and gas components of cluster galaxies (also known as harassment, Moore *et al.* 1996). Gas falling onto a cluster is heated by shocks leading to a hot, diffuse intracluster medium (ICM) which permeates the space between the galaxies. The ICM can impact the gas within a galaxy by either compressing it, leading to triggered star formation (Bekki & Couch 2003), or by removing the galaxy gas which is required to fuel star formation and leading to a quenching of star formation. This process is known as ram-pressure stripping (Gunn & Gott 1972). Both ram-pressure and tidal stripping by the halo potential can remove the hot gas halo surrounding the galaxy (the so-called strangulation, Larson, Tinsley & Caldwell 1980; Balogh, Navarro & Morris 2000).

Disentangling the relative importance of these processes in transforming an infalling galaxy has been the subject of much

debate. Detailed studies of galaxies affected by cluster specific processes are made possible by the signature that each process is expected to leave on the spatial distribution of the star formation activity within the galaxy. For example, ram pressure is expected to partially or completely strip layers of gas from a galaxy, leaving a recognizable pattern of star formation with truncated $H\alpha$ disks smaller than the undisturbed stellar disk (e.g., Yagi *et al.* 2015). Strangulation, depriving the galaxy of its gas reservoir and leaving the existing interstellar medium (ISM) in the disk to be consumed by star formation, should instead produce a symmetric pattern. Other processes, like strong tidal interactions and mergers, tidal effects, harassment, thermal evaporation (Cowie & Songaila 1977), and turbulent/viscous stripping (Nulsen 1982) can also deplete the gas in a non-homogeneous way, leaving non-symmetric $H\alpha$ disks.

Understanding the transformation process has been further complicated by our lack of understanding of the impact of cluster growth on galaxies. Hierarchical cluster growth occurs via both continuous infall of material from the surrounding filaments and high impact merging of two approximately equal mass clusters. Simulations indicate that a significant fraction of both the mass and galaxies in clusters at the current epoch have been accreted through minor and major cluster mergers ($\sim 50\%$ Berrier *et al.* 2009; McGee *et al.* 2009). Therefore, it is important to understand the impact of this process on the available gas and the galaxies. Simulations show that the high ICM pressure a galaxy experiences during the core-passage phase of a merger can trigger star formation (Bekki, Owers & Couch 2010) while the high relative velocity of ICM and galaxies can enhance ram-pressure stripping of the ISM, leading to a sharp truncation of star formation (Fujita *et al.* 1999). Since the timescales for the star forming phases of galaxies (1–100 Myr) are shorter than typical merger timescales (\sim Gyrs), a detailed understanding of the dynamics and merger stage of the cluster are crucial when attempting to interpret the observed galaxy populations.

In this paper we extend the analysis presented by Vulcani *et al.* (2015, hereafter Paper V) and Vulcani *et al.* (2016, hereafter Paper VII) and investigate whether cluster properties are able to affect the extent and spatial distribution of the $H\alpha$ emitters in the 10 Grism Lens-Amplified Survey from Space (GLASS; GO-13459; PI: Treu,¹ Schmidt *et al.* 2014; Treu *et al.* 2015) clusters at $0.3 < z < 0.7$. We use resolved spectral information to characterize the gaseous material that has been stripped from the galaxy disk by any process. We therefore address how star formation is suppressed and look for signs of a dependence of the suppression on cluster morphology.

In Paper V, we illustrated the methodology by focusing on two clusters (MACS0717.5+3745 and MACS1423.8 +2404) with different morphologies (one relaxed and one merging) and used foreground and background galaxies as a field control sample, for a total of 42 galaxies. We investigated trends with the hot gas density as traced by the X-ray emission, and with the surface mass density as inferred from gravitational lens models and found no conclusive results. The diversity of morphologies and sizes observed in $H\alpha$ illustrated the complexity of the environmental process that regulate star formation. In Paper VII we increased the sample size and used 76 galaxies in clusters and 85 galaxies in the field to compare the spatial distribution of star formation in galaxies in the two most different environments. Here we focus on galaxies in

clusters and investigate how the $H\alpha$ morphology and the main process thought to be responsible for the $H\alpha$ appearance depend on the clustercentric distance, the hot gas density, the surface mass density and the local density. Our goal is to use these sensitive diagnostics to achieve better insight on the role of the cluster environment in driving galaxy transformations.

The paper is structured as follows. §2 introduces the dataset and the clusters, §3 presents the galaxy properties. §4 presents the main results of this study: we characterize $H\alpha$ morphologies as a function of clustercentric distance (§4.1) and compare the observed distribution of the projected offsets to cosmological predictions of the orbits of infalling galaxies (§4.1.1). We then characterize $H\alpha$ morphologies as a function of global (§4.2) and local (§4.3) cluster properties and the variation of the specific star formation rate (SFR) with environment (§4.4). In §5 we discuss our results and conclude.

We assume $H_0 = 70 \text{ km s}^{-1} \text{ Mpc}^{-1}$, $\Omega_0 = 0.3$, and $\Omega_\Lambda = 0.7$. We adopt a Chabrier (2003) initial mass function (IMF) in the mass range 0.1–100 M_\odot .

2. THE GRISM LENS-AMPLIFIED SURVEY FROM SPACE

2.1. The dataset

GLASS is a 140-orbit slitless spectroscopic survey with *HST* in cycle 21. It has observed the cores of 10 massive galaxy clusters targeted by the Hubble Frontier Fields (HFF; P.I. Lotz, Lotz *et al.* 2016) and by the Cluster Lensing And Supernova survey with Hubble (CLASH; P.I. Postman, Postman *et al.* 2012) with the Wide-Field Camera 3 (WFC3) Near Infrared (NIR) grisms G102 and G141 providing an uninterrupted wavelength coverage from $0.8 \mu\text{m}$ to $1.7 \mu\text{m}$. Each cluster was observed at two position angles (PAs) approximately 90 degrees apart to facilitate clean extraction of the spectra for objects in the crowded cluster fields. The sample of 10 clusters and their properties is presented in Table 1.

Details on the observations and data reduction can be found in Schmidt *et al.* (2014); Treu *et al.* (2015). Briefly, observations follow the dither pattern used for the 3D-HST observations and were processed with an updated version of the 3D-HST reduction pipeline² described by Brammer *et al.* (2012); Momcheva *et al.* (2015). All spectra were visually inspected with the publicly available GLASS inspection GUI, GiG³ (Treu *et al.* 2015), in order to identify and flag erroneous models from the reduction, assess the degree of contamination in the spectra and flag and identify strong emission lines and the presence of a continuum.

As described in Treu *et al.* (2015), to determine redshifts, templates were compared to each of the four available grism spectra independently (G102 and G141 at two PAs each) to compute a posterior distribution function for the redshift. Then, with the help of the publicly available GLASS inspection GUI for redshifts (GiGz, Treu *et al.* 2015), we flagged which grism fits are reliable or alternatively entered a redshift by hand if the redshift was misidentified by the automatic procedure. Using GiGz we assigned a quality Q_z to the redshift (4=secure; 3=probable; 2=possible; 1=tentative, but likely an artifact; 0=no- z). These quality criteria take into account the signal to noise ratio of the detection, the possibility that the line is a contaminant, and the identification of the feature with a specific emission line. This procedure was carried out independently by at least two inspectors per cluster (see Treu *et al.* 2015, for details).

¹ <http://glass.astro.ucla.edu>

² <http://code.google.com/p/threedhst/>

³ github.com/kasperschmidt/GLASSinspectionGUIs

TABLE 1
CLUSTER PROPERTIES

cluster	short name	RA (J2000)	DEC (J2000)	z	phys scale (kpc'')	L _X (10 ⁴⁴ erg s ⁻¹)	M ₅₀₀ (10 ¹⁴ M _⊙)	r ₅₀₀ (Mpc)	PA1	PA2
Abell2744	A2744	00:14:21.2	-30:23:50.1	0.308	4.535	15.28±0.39	17.6±2.3	1.65±0.07	135	233
RXJ2248.7-4431	RXJ2248	22:48:44.4	-44:31:48.5	0.346	4.921	30.81±1.57	22.5±3.3	1.76±0.08	053	133
Abell370	A370	02:39:52.9	-01:34:36.5	0.375	5.162	8.56±0.37	11.7±2.1	1.40±0.08	155	253
MACS0416.1-2403	MACS0416	04:16:08.9	-24:04:28.7	0.420	5.532	8.11±0.50	9.1±2.0	1.27±0.09	164	247
RXJ1347.5-1145	RXJ1347	13:47:30.6	-11:45:10.0	0.451	5.766	47.33±1.2	21.7±3.0	1.67±0.07	203	283
MACS1423.8+2404	MACS1423	14:23:47.8	+24:04:40	0.543	6.382	13.96±0.52	6.64±0.88	1.09±0.05	008	088
MACS1149.6+2223	MACS1149	11:49:36.3	+22:23:58.1	0.544	6.376	17.25±0.68	18.7±3.0	1.53±0.08	032	125
MACS0717.5+3745	MACS0717	07:17:31.6	+37:45:18	0.546	6.400	24.99±0.92	24.9±2.7	1.69±0.06	020	280
MACS2129.4-0741	MACS2129	21:29:26.0	-07:41:28.0	0.589	6.524	13.69±0.57	10.6±1.4	1.26±0.05	050	328
MACS0744.9+3927	MACS0744	07:44:52.8	+39:27:24.0	0.686	7.087	18.94±0.61	12.5±1.6	1.27±0.05	019	104

NOTE. — J2000 coordinates, redshift, physical scale, X-ray luminosity, M₅₀₀ (from Mantz *et al.* 2010), r₅₀₀ and the two position angles.

The full redshift catalogs from the inspection of the 10 GLASS clusters are available at <https://archive.stsci.edu/prepds/glass/>.

2.2. The clusters

We make use of all 10 GLASS clusters. Virial radii r_{500} have been computed from virial masses M_{500} taken from Mantz *et al.* (2010):

$$r_{500} = \sqrt[3]{\frac{3}{4\pi} \frac{M_{500}}{500\rho_{cr}}}$$

where $\rho_{cr} = \frac{3H_0^2}{8\pi G} = \frac{3H_0^2}{8\pi G} \times [\Omega_\Lambda + \Omega_0 \times (1+z)^3]$, with G being the gravitational constant = $4.29 \times 10^{-9} (\text{km/s})^2 \text{Mpc} M_\odot$.

Clustercentric distances have been computed in units of r_{500} from the peak of the X-ray distribution. For merging clusters, where more than one peak in the X-ray distribution can be detected, distances have been computed from the closest peak. Cluster mass maps were produced using the SWUnited reconstruction code described in detail in Bradač *et al.* (2005) and Bradač *et al.* (2009). The method uses both strong and weak lensing mass reconstruction on a non-uniform adapted grid. From the set of potential values we determine all observables (and mass distribution) using derivatives. The potential is reconstructed by maximizing the log likelihood which uses image positions of multiply imaged sources, weak lensing ellipticities, and regularization as constraints. Our team has at disposal the cluster mass maps for all clusters, except for MACS0744, which is not ready yet. The X-ray images are based on Chandra data, and are described in Mantz *et al.* (2010) and von der Linden *et al.* (2014). For the contours, the images have been adaptively smoothed, after removing point sources identified in Ehlert *et al.* (2013). X-ray images are available for all clusters. For estimating the X-ray emission at the location of the galaxy, we masked the galaxy itself (which can emit in X-rays) and computed the average signal in an annulus around the galaxies with inner radius 2'' and outer radius 5''.

The local density of a galaxy is defined as the number of its neighbors per unit projected area: $\Sigma = N/A$ in number of galaxies per Mpc^{-2} . The projected number densities have been estimated from the circular area containing the 5 closest objects: $\Sigma = (5+1)/\pi r_5^2$, with r radius of such area (see Morishita *et al.* 2016). Local density estimates are available for only 4 clusters in our sample, A2744, MACS0416, MACS0717, and MACS1149, which are the first HFF clusters with complete data.

TABLE 2
NUMBER OF GALAXIES WITH H α IN EMISSION IN EACH CLUSTER

cluster	cluster members
A2744	4
RXJ2248	3
A370	8
MACS0416	2
RXJ1347	2
MACS1423	10
MACS1149	8
MACS0717	16
MACS2129	8
MACS0744	15
total	76

3. H α MAPS AND GALAXY PROPERTIES FROM PAPER XI

The entire sample and its properties are presented in detail in Paper VII. Briefly, from the redshift catalogs, we extract galaxies with secure redshift and consider as cluster members galaxies with redshift within ± 0.03 of the cluster redshift.⁴ Then, we select galaxies with visually detected H α in emission. We exclude the Brightest Cluster galaxies (BCGs) from our analysis, which are not representative of the general cluster galaxy population.

Overall, our sample includes 76 H α -emitting cluster galaxies, distributed among the different clusters as summarized in Table 2. We note that since the GLASS dataset does not typically yield redshifts for cluster passive galaxies (the 4000Å break is too blue for the setup).

3.1. Methodology

3.1.1. H α maps

Slitless grism observations have high spatial resolution and low spectral resolution, and therefore provide images of galaxies in the light of their emission lines for every object in the field of view. The details of the procedure we followed to make emission line maps of galaxies are described in Paper V. Briefly, the H α emission line maps are made, separately for each PA, by subtracting the continuum from the two-dimensional spectra and masking contaminating flux from nearby objects. We then superimposed the H α map onto an image of the galaxy taken with the F475W filter (rest-frame UV) and onto an image in the F140W (IR). Images are taken from the HFF (Lotz *et al.* 2016) or CLASH HST (Postman *et*

⁴ The limit 0.03 is given at 3σ , corresponding to a $1-\sigma$ dispersion of 1000 km/s. This choice is driven by the uncertainty in grism-based redshifts owing to limited resolution, of order 0.01.

al. 2012) programs. We use the F475W filter to map relatively recent (~ 100 Myr) star formation, and the F140W to trace the older stellar population; as opposed to ongoing (~ 10 Myr) star formation traced by $H\alpha$. Note that for A2744 we used the F435W filter instead, because the F475W filter is not available.

We aligned each map to the continuum image of the galaxy, rotating each map by the angle of its PA, keeping the y -offset unaltered with respect to the continuum. In the dispersion direction, there is a degeneracy between the spatial dimension and the wavelength uncertainty, it is therefore not possible to determine very accurately the central position of the $H\alpha$ map for each PA separately. However, for the cases in which spectra from both PAs are reliable, which are the vast majority, we used the fact that the 2 PAs differ by almost 90° , therefore the x -direction of one spectrum roughly corresponds to the y -direction of the second spectrum and vice-versa. We shifted the two spectra independently along their x -direction to maximize the cross correlation between the two maps to get the intersect. For the galaxies with reliable spectra in both PAs, we also measured the real distance between the peak of the $H\alpha$ emission and the continuum emission, obtained as the quadratic sum of the two offsets.

We also measured the magnitude of the offset between the $H\alpha$ and the continuum as projected along the cluster radial (off_r) and tangential (off_θ) directions, determined by the line connecting the cluster center and the galaxy center in the continuum light. In merging clusters, where more than one cluster center has been identified, the closest one to each galaxy is adopted. We assigned a positive sign to the radial offset when the peak of the $H\alpha$ is between the cluster center and the peak of the continuum.

3.1.2. Additional galaxy properties

Table 3 in Paper VII summarizes the main galaxy properties that are used also in this analysis. Briefly, stellar mass estimates have been derived using FAST v.1.0 (Kriek *et al.* 2009) using the spectroscopic redshift of each object. CLASH (Postman *et al.* 2012) or, when available, HFF photometry (Lotz *et al.* 2016) has been adopted. For details on stellar mass estimates refer to Morishita *et al.* (2016).

The stellar population properties have not been fitted for A370, since the final HFF observations were not available while this study was carried out.

The surface SFR density (ΣSFR , $M_\odot \text{ yr}^{-1} \text{ kpc}^{-2}$) and the total SFRs ($M_\odot \text{ yr}^{-1}$), have been derived from $H\alpha$ maps. The total SFRs are obtained summing the surface SFR density within the Kron radius measured by SExtractor from a combined NIR image of the galaxy. We used the conversion factor derived by Kennicutt, Tamblyn & Congdon (1994) and Madau, Pozzetti & Dickinson (1998) and corrected SFR estimates for both the scatter due to the [NII] contamination, applying the locally calibrated correction factor given by James *et al.* (2005) and dust extinction, using the relation given by Garn & Best (2010).

As described in Paper VII, our ΣSFR limit is around $5 \times 10^{-2} M_\odot \text{ yr}^{-1} \text{ kpc}^{-2}$ for $\text{SFR} \sim 1 M_\odot \text{ yr}^{-1}$ and we use this value as indication of the completeness limit of our sample.

Visual classification of galaxy broad-band morphology in the continuum and of the $H\alpha$ line have been performed as presented in Paper VII using the publicly available GLASS inspection GUI for morphologies (GiGm).⁵ Galaxies have

been subdivided into Ellipticals (E), Lenticulars (S0), Spirals (Sp), Mergers (Mer) and Irregulars (Irr) and in $H\alpha$ regular, $H\alpha$ clumpy, $H\alpha$ concentrated, $H\alpha$ asymmetric/jellyfish.

We also attempted to classify the most likely physical processes responsible for altering its continuum and $H\alpha$ morphology. Five main processes have been proposed: regular, ram pressure, major mergers, minor mergers/interaction and other (when none of the above applies). This is clearly a qualitative and approximate classification scheme, considering that multiple processes might be simultaneously at work and that the mapping between morphology and process is not always unique and unambiguous. As discussed in Paper VII, in spite of the uncertainties, we believe there is merit in categorizing in a self consistent manner the diversity of morphological features across environments. In the future, this classification scheme might be replaced with full 2D comparisons with numerical simulations. However, a qualitative visual classification appears to be a useful first step. In general, we assigned to the regular class galaxies with regular and undisturbed $H\alpha$ light distribution, to the ram pressure class galaxies where an asymmetry in the $H\alpha$ distribution or in the surface brightness is detected. We were not able to detect weak cases of ram-pressure stripping, for example when a galaxy is at its second or third passage toward the cluster center, but only the strongest ones, when large quantities of gas are still available, and the ionized gas is stripped away in a direction that approximately points away from the cluster center. Even though the inspection was not done blindly with respect to the environment, we did not explicitly take into account the location of the galaxies with respect to the cluster center to characterize this process; we distinguished between major and minor merger by looking at the same galaxies in the different bands: in major mergers the constituents of the mergers are visible both in the F140W and F475W filters, suggesting they are both massive and luminous; while in minor mergers the F475W filter shows the presence of material infalling onto the main galaxies that is not detected in the F140W filter, suggesting that, though luminous, such infalling material is not very massive. Examples of the different cases are shown in Paper VII.

4. RESULTS

The focus of the current paper is to correlate the properties of the $H\alpha$ emitters to the properties of the clusters in which they are embedded, as opposed to Paper VII where we looked at the differences between cluster and field galaxies. We refer the reader to Paper VII for an exhaustive analysis of the $H\alpha$ distribution in the different environments.

4.1. $H\alpha$ morphologies as a function of cluster-centric distance

We characterize the spatial distribution of the $H\alpha$ emitters in terms of cluster-centric distance. We note that since the GLASS dataset does not yield redshifts for passive galaxies, we can not characterize the spatial distribution of all cluster members. The upper left panel of Figure 1 shows that galaxies are located within $\sim 0.5 r_{500}$, that roughly corresponds to the maximum coverage of all the clusters, and do not seem to avoid the cluster cores, even though there might be possible projection effects. The distribution peaks around $0.2 r_{500}$. We distinguish between relaxed (MACS1423, RXJ1347, MACS2129, RXJ2248, MACS0744, for a total of 38 galaxies) and merging/unrelaxed (MACS1149, MACS0717, A2744, MACS0416, A370, for a total of 38 galaxies) clusters. Since

⁵ <https://github.com/kasperschmidt/GLASSinspectionGUIs>

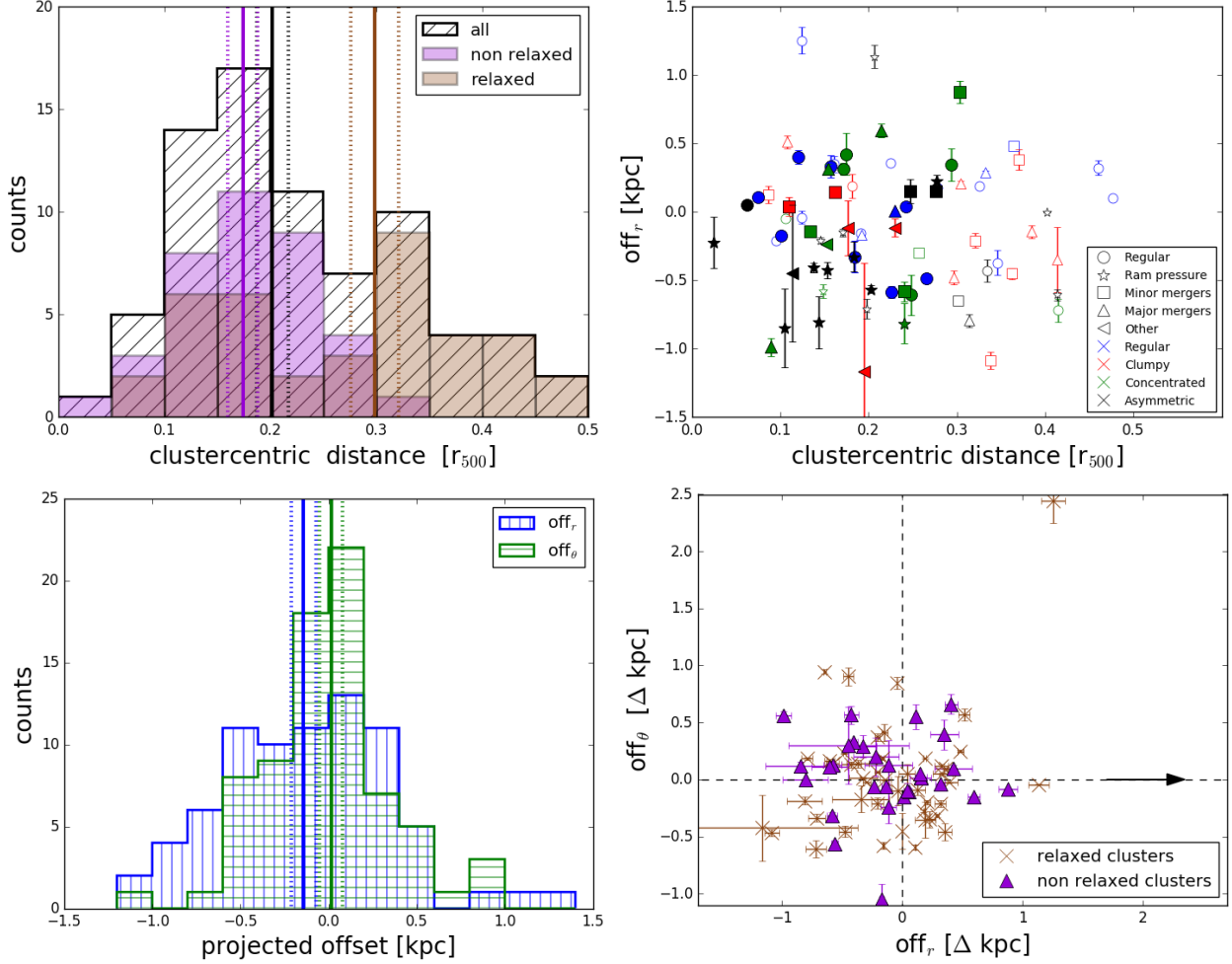


FIG. 1.— *Upper left*: Clustercentric distribution of all H α emitters. All galaxies (black), galaxies in unrelaxed clusters (purple) and galaxies in relaxed clusters (brown) are shown. The median value with errors on the median ($1.235 \times \sigma / \sqrt{n}$) is also shown. *Upper right*: Radial projected offset (off_r) as a function of clustercentric distance, for galaxies with different H α morphology (colors) and experiencing different physical processes (symbols), as indicated in the label. Galaxies in unrelaxed clusters are shown as filled symbols, galaxies in relaxed clusters as empty symbols. *Bottom left*: radial (blue) and tangential (green) projected offsets. Median values along with errors are also shown. *Bottom right*: Correlation between the tangential and radial projected offset for galaxies in relaxed (red crosses) and non relaxed (purple triangles) clusters. The black arrow, located at an arbitrary distance, indicates the direction of the cluster centers, the dashed cross the UV-continuum light center of the galaxies. H α emitters lie at all distances from the cluster centers, peaking around $r/r_{500} \sim 0.2$. Galaxies in unrelaxed clusters are typically closer to the center than galaxies in unrelaxed ones. While the typical tangential offset has a Gaussian distribution peaked at $\Delta off_\theta = 0$, the distribution of radial offsets is skewed toward negative values, indicating that H α typically points away from the cluster center. The extent of the offset does not correlate to clustercentric distances, but there are hints that the offset correlates with some physical processes (e.g. ram-pressure stripped galaxies have a more negative offset).

there is no a unique and clear criterium to distinguish between the two categories, we assume that in unrelaxed clusters more than one X-ray peak is detected, as it will be discussed in Section 4.2. Galaxies in unrelaxed clusters tend to be located closer to the cluster center than galaxies in relaxed clusters. Recall that for merging systems, where more than one peak in the X-ray distribution can be detected, distances have been computed from the closest peak. The median value for the former is 0.17 ± 0.01 , that for the latter is 0.30 ± 0.02 . We have also checked for mass segregation and computed the mean and median galaxy masses in bins of distance. We found that the typical stellar mass is similar at all distances from the cluster center, suggesting that the mass build-up is not very sensitive to the position of the galaxy in the cluster.

The upper right panel of Figure 1 quantifies the relation between the radial offset (i.e. the offset between the peak of the H α emission and the peak in the F475W filter projected along the cluster radial direction) and the distance of the galaxy from the cluster center. Most of the galaxies have offset within ± 0.5 kpc, but there are some showing a larger offset. The

typical uncertainty on the offset estimates is ~ 0.1 kpc. When considering the entire galaxy population as a whole, no dependencies on the cluster-centric distances are detected (Spearman correlation = -0.008 with 94% significance). Galaxies in relaxed and unrelaxed clusters have similar offsets. As also seen in the bottom left panel, 60% of cluster H α emitters have negative radial projected offset and the distribution is clearly shifted towards negative values (the median of the distribution is -0.14 ± 0.07 kpc), indicating that for most of the galaxies the H α peak points away from the cluster center. This finding might suggest that our galaxies are approaching the cluster center for the first time, and the weakly bound gas is left behind. However, the analysis of the skewness does not support the result: the ratio of the skewness to the Standard Error of Skewness (SES)⁶ is $0.23/0.24 \sim 0.83$, suggesting that population data are neither positively or negatively skewed.

⁶ The statistical formula for Standard Error of Skewness (SES) for a normal distribution is $SES = \sqrt{\frac{6n(n-1)}{(n-2)(n+1)(n+3)}}$.

We will revisit and try to test quantitatively this hypothesis in the next section. In contrast, the distribution of the tangential offset peaks around 0 (the median of the distribution is 0.01 ± 0.07 kpc, skewness/SES = $0.15/0.24 \sim 0.62$), indicating no preferential direction. A K-S test confirms that the two distributions are different (i.e. 4% probability of being drawn from the same parent distribution). If we consider only the 39/76 galaxies for which we have two orthogonal spectra and therefore the offset is better constrained, we find the same trends, indicating our results are robust against uncertainties. No strong differences are found for galaxies in relaxed and unrelaxed clusters.

The bottom right panel of Figure 1 correlates the tangential to the radial offset. As already noticed, there is no preferential direction for the tangential offset, while the radial offset is directed away from the cluster center. No differences emerge for relaxed and unrelaxed clusters

Galaxies with different H α morphologies and experiencing different physical processes are highlighted in the upper right panel of Figure 1. Ram-pressure stripped galaxies with asymmetric morphology are preferentially found between 0.1 and 0.3 r_{500} , and tend to have negative radial offset, indicating that in these galaxies the H α distribution is strongly influenced and shows a systematically different distribution than the existing stellar population. In contrast, galaxies of the other types are not clustered.

4.1.1. Comparison of galaxy infall to cosmological simulations

In the previous Section we have found that the magnitude of the offset might give us an indication on the process operating on galaxies. In addition, it might also carry information about the orbit along which a galaxy is traveling through the ICM. In particular, if the offset is due to ram pressure, its direction is expected to trace the direction of the galaxy velocity. Therefore, the ratio $\text{off}_r/|\text{off}_\theta|$ between the radial and the tangential offsets can be taken as a proxy for the ratio $v_r/|v_\theta|$ between the radial and the one-dimensional tangential components of the galaxy velocity at the time of the observation (v_r and v_θ are two of the three components of the velocity vector in spherical coordinates). As off_r is defined so that it is positive when the peak of the H α emission is closer to the cluster centre than the continuum emission, we expect that an infalling galaxy ($v_r < 0$) has negative off_r . In this Section we compare our observed radial and tangential offsets to the cosmological predictions of the orbits of infalling satellites onto galaxy clusters. For simplicity in what follows we just identify $\text{off}_r/|\text{off}_\theta|$ with $v_r/|v_\theta|$, neglecting all possible sources of difference between the two quantities (for instance the offset ratio is a projected quantity, while the velocity ratio is an intrinsic quantity). We note that the proxy is an underestimate of the real offset, since we would not measure any offset for objects which are infalling along the line of sight, yet they would have large v_r/v_θ .

As reference for the cosmological predictions we take the results of Jiang *et al.* (2015), who studied the distribution of the orbital parameters of infalling satellite halos in a Λ cold dark matter (ACDM) cosmological N -body simulation. In particular Jiang *et al.* (2015) provide the distributions of V/V_{200} and V_r/V as functions of host-halo mass and satellite-to-host halo mass ratio, where V is the satellite's speed at r_{200} , V_r is the radial component of the satellite's velocity at r_{200} and V_{200} is the host-halo circular velocity at r_{200} . Jiang *et al.* (2015) parameterize the distribution of V/V_{200} with the three

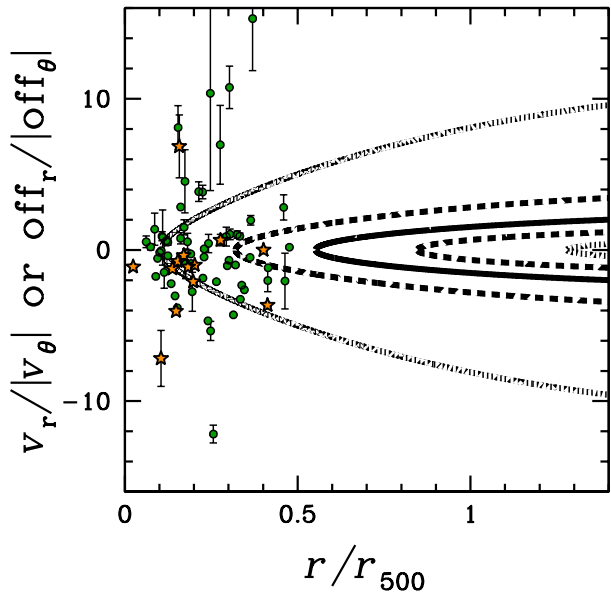


FIG. 2.— Observed projected radial-to-tangential offset ratio $\text{off}_r/|\text{off}_\theta|$ as a function of distance from the cluster centre. The stars represent the galaxies belonging to the ram-pressure class, while the other galaxies are represented by circles. Note that four galaxies are not shown because they have $|\text{off}_r/|\text{off}_\theta| > 16$. Radial-to-tangential velocity ratio $v_r/|v_\theta|$ as a function of radius for characteristic orbits of the cosmological satellite orbit distribution estimated by Jiang *et al.* (2015) are shown as the various curves. The orbits correspond to the following percentiles of the predicted distribution of V_r/V (where V is the speed and V_r is the radial component of the velocity at r_{200}): 50th (solid curve), 25th and 75th (dashed curves), and 5th and 95th (dotted curves). The observed sample of cluster galaxies traces only the $\sim 25\%$ most radial orbits of the cosmological distribution.

dimensionless parameters γ , σ and μ , and the distribution of V_r/V with the dimensionless parameter B (see section 3.4 in that paper). Here we fix $\gamma = 0.05$, $\sigma = 0.118$, $\mu = 1.236$, and $B = 3.396$, which are the best-fitting values for host-halo mass $10^{14} M_\odot$ and satellite-to-host mass ratio 0.05-0.005 from Jiang *et al.* (2015) (note, however, that our results are not strongly dependent on this specific choice).

Assuming that the host halo is spherical and exploiting the fact that energy and angular momentum are conserved (neglecting tidal stripping and dynamical friction), for each orbit of given V/V_{200} and V_r/V it is straightforward to compute the ratio $v_r/|v_\theta|$, at each radius $r < r_{200}$. Specifically, we assumed that the host halo has a NFW (Navarro, Frenk & White 1996) density distribution with concentration $c_{200} = 4$ (in this case $r_{500}/r_{200} \simeq 0.65$).

As a first comparison between the cosmological predictions and the observations, we look at the behavior of the offset and velocity ratios as functions of distance from the cluster centre (for simplicity here we identify the projected observed cluster distance with the intrinsic orbital radius r). In Figure 2 the radial distribution of the observed offset ratios is compared with a few orbits characteristic of the cosmological orbit dis-

tribution. Since Jiang *et al.* (2015) find that the distribution of V/V_{200} is relatively narrow, for simplicity, to compute the theoretical curves in Figure 2, we fix $V/V_{200} = 1.236$ (the average value of the best fit of the distribution) and we sample the distribution in V_r/V by selecting orbits corresponding to the 5th, 25th, 50th, 75th and 95th percentiles. Figure 2 shows, as expected, that the observed sample (confined within $r/r_{500} < 0.5$) traces only the $\approx 25\%$ most radial orbits of the cosmological distribution: the bulk of the cosmological orbits do not plunge deep enough into the cluster potential (see also Crane & Saslaw 1986). One caveat is that in the analysis above we have neglected dynamical friction. However, this effect is negligible, at least for the first pericentric passage, as we verified by running N -body simulations for all the orbits represented in Figure 2. In these simulations, run with the collisionless N -body code FVFPs (Londrillo, Nipoti & Ciotti 2003; Nipoti, Londrillo & Ciotti 2003), we have followed, starting from r_{500} , the orbit of an infalling galaxy, represented as a particle with mass $0.005M_{200}$, in an isotropic NFW halo with concentration $c_{200} = 4$, realized with $N \simeq 10^6$ particles (M_{200} is the total mass of the halo, which is truncated exponentially at r_{200}). The set-up and technical characteristics of these simulations are identical to those described by Nipoti (2017).

Figure 2 suggests that the observed H α cluster galaxies might represent the radial-orbit selected tail of the distribution of cosmological satellites. If the cosmological prediction is correct, and if $\text{off}_r/|\text{off}_\theta|$ is a proxy for $v_r/|v_\theta|$, at each radius $\text{off}_r/|\text{off}_\theta|$ should be distributed as the predicted $v_r/|v_\theta|$. To verify whether this is actually the case, we select, among the observed galaxies only the subsample (44 galaxies) with $\text{off}_r < 0$, that, under our hypothesis, are infalling galaxies, for which the mapping between $\text{off}_r/|\text{off}_\theta|$ and $v_r/|v_\theta|$ should be more justified. In principle $\text{off}_r/|\text{off}_\theta|$ might be a proxy for $v_r/|v_\theta|$ also for galaxies that are receding from the centre of the cluster ($v_r > 0$), but this model is too simple to describe a system that has already passed the pericenter. For comparison with this subsample we generate a sample of 4400 mock galaxies with the same radial distribution. The orbital parameters of these mock galaxies are extracted from the distributions of V/V_{200} and V_r/V given by Jiang *et al.* (2015) with the values of the parameters reported above. The mock sample of galaxies can be used to numerically compute the distribution of $v_r/|v_\theta|$ at each observed radius to be compared with the observed values of $\text{off}_r/|\text{off}_\theta|$. In order to verify whether the observed and mock samples are consistent, we first compute the probability distribution of $\text{off}_r/|\text{off}_\theta|$ for the 44 observed galaxies and the probability distribution of $v_r/|v_\theta|$ for the 4400 mock galaxies. From Figure 3a, where these distributions are plotted, it is apparent that there is qualitative agreement between the observed and theoretical histograms. When the cumulative distributions are considered (inset in Figure 3b), there appears to be a discrepancy for large values $|\text{off}_r/|\text{off}_\theta|$ and $|v_r/|v_\theta|$ ($x \lesssim -5$), but this discrepancy is not statistically significant, because the number of observed galaxies in this tail of the distribution is small (see Figure 3c). This can be quantified with a K-S test, which gives a probability of 51% that the two samples are extracted from the same parent population. As a further statistical test, for each galaxy of the sample we computed how it ranks within the distribution of mock galaxies at the same radius. If the distributions are consistent the quantiles must be distributed uniformly. According to the K-S test, the probability that the quantiles are extracted from a uniform distribution is 25%.

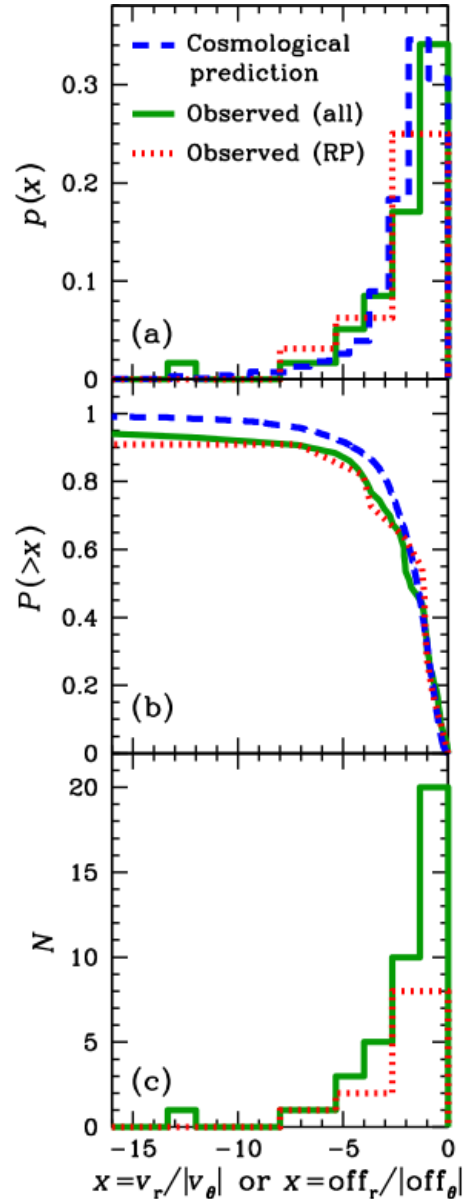


FIG. 3.— *Panel a.* Probability distribution (p) of the observed radial-to-tangential offset ratio $\text{off}_r/|\text{off}_\theta|$ for the 44 galaxies in our sample with negative off_r (solid curve; sample “all”) and for the sub-sample of 12 galaxies belonging to the ram-pressure class (dotted curve; sample “RP”). The dashed curve represents the probability distribution of the radial-to-tangential velocity ratio $v_r/|v_\theta|$ for the mock sample of infalling ($v_r < 0$) galaxies with the same radial distribution as sample “all”. At fixed radius, the values of v_r and $|v_\theta|$ are generated by following orbits that at r_{200} have the orbital parameter distribution estimated by Jiang *et al.* (2015) from a Λ CDM N -body simulation. The distribution of $v_r/|v_\theta|$ of the mock galaxies of the sample “RP”, not shown, is almost indistinguishable from that of the mock galaxies of sample “all”. *Panel b.* Cumulative distributions (P) of the two observed samples and of the cosmological prediction. *Panel c.* Number of galaxies per bin of $\text{off}_r/|\text{off}_\theta|$ for the two observed samples (the bins are those used in panel a).

We repeated the above analysis for the subsample of 12 galaxies with $\text{off}_r < 0$ that we visually classified as affected by ram-pressure stripping (see Sec. 3.1.2, stars in Figure 2), for which our model is expected to work best (in this case we created a mock sample of 1200 galaxies). We find again that the cumulative distribution of the offset ratios (Figure 3b) is consistent with the theoretical expectation, as supported by the K-S test, which gives a probability of 71% that the two samples (mock and observed) are extracted from the same parent population. In this case the probability that the distribution of

the quantiles is uniform is 48%.

Bearing in mind the small sample size, we conclude that the observed distribution of offset ratios for the infalling galaxies is consistent with the cosmological predictions. This finding is even more significant when we consider only the infalling galaxies we labeled as affected by ram-pressure stripping, therefore cosmological predictions support our classification scheme.

4.2. $H\alpha$ morphologies as a function of hot gas density and surface mass density

Over the last years, there has been increasing evidence for a correlation between the efficiency of the stripping phenomenon and the presence of shocks and strong gradients in the X-ray IGM (e.g., Owers *et al.* 2012; Vijayaraghavan & Ricker 2013). In Paper V we found tentative trends between the X-ray counts and the radial offset, even though correlations were not supported by statistical tests.

Figure 4 presents the color composite images of all our clusters along with X-ray maps. Clearly, the clusters in our sample present very different X-ray emission morphologies: RXJ1347, RXJ2248, MACS1423, MACS2129, and MACS0744 show quite symmetric emissions and are relaxed, while A2744, A370, MACS0416, MACS1149, and MACS0717 have more than one main peak and extend along the north-south direction (A370), the north-west - south-east direction (A2744, MACS0717, MACS1149), or the north-east - south-west direction (MACS0416). $H\alpha$ emitters with different $H\alpha$ morphologies and experiencing different processes are highlighted.

Galaxies with all kinds of $H\alpha$ morphologies and also experiencing all the proposed physical processes are found in almost all clusters. Due to the low number statistics in each cluster, it is hard to detect solid trends with morphology and acting process. In MACS1423, $H\alpha$ emitters are almost all the same clustercentric distance, where the hot gas density is nearly constant. However, this is not the case for the other relaxed clusters. In A2744 and MACS0717, characterized by multiple centers, $H\alpha$ emitters tend to lie all in the same region of the cluster, and avoid the second peak. In MACS0416 there are only two $H\alpha$ emitters, therefore no solid conclusion can be drawn. The same is true for RXJ1347 and RXJ2248.

It is worth noting that some galaxies are found correspondence of a peak in the X-ray distribution, such as in MACS0744. However, in this case, the $H\alpha$ morphology seems not to be affected by its peculiar position: indeed it has been visually classified as a galaxy with a regular $H\alpha$ morphology where no strong process is occurring. We remind the reader that the classification has been performed blindly with respect to the cluster properties.

We note that we cannot know the exact three-dimensional locations of the galaxies with respect to the ICM structures, but in some cases the small projected distances from the X-ray peaks and shocks suggest that some galaxies may have recently been overrun by the shock front subcluster gas. This indicates that a mechanism related to an interaction with these ICM features may be in some cases responsible for either the stripping of the gas or the triggering of the star formation, or both.

Similarly, Figure 5 shows the color composite images of 9 of our clusters for which the surface mass density maps are available (see §2.2). These maps, based on lens modeling, provide an estimate for the total mass density of the cluster, composed mostly of invisible dark matter. Also from these

maps the variety of structures in our sample emerges: A370, MACS0717, MACS1149, A2744 and MACS0416 present more than one peak in their distribution, the former extending along the north-west - south-east direction, the latter along the north-east - south-west direction. In contrast, MACS1423, MACS2129, RXJ2248 and RXJ1347 show nearly symmetric mass distribution.

Figure 6 correlates the projected radial offset with both the X-ray emission and the surface mass density. X-ray surface brightness has been corrected for cosmological dimming ($\propto (1+z)^4$). In both cases, Spearman rank-order correlation tests show that no correlation is present between these quantities (Spearman correlation=0.004 with 80% significance). However, if we consider only galaxies in unrelaxed clusters, a weak correlation seems to emerge, in the sense that galaxies at higher X-ray counts and surface mass densities tend to have more negative offsets. The Spearman correlation test supports these findings. This result might suggest that in merging systems X-ray counts are a proxy for mergers between substructures (see, e.g. Poggianti *et al.* 2004), while in the relaxed ones they simply trace the density of the ICM, without inducing an alteration in galaxy properties.

In addition, galaxies in unrelaxed clusters tend to be located systematically at higher X-ray counts and tend to avoid lower surface mass densities than galaxies in all clusters, indicating that in merging systems the gas temperature and the total dark matter are larger.

Trends with $H\alpha$ morphology or acting process are hardly detected, both in relaxed and unrelaxed clusters. Few $H\alpha$ asymmetric, ram-pressure stripped candidates are indeed at high values of the X-ray emission (in agreement with Owers *et al.* 2012; Vijayaraghavan & Ricker 2013), but we find others at intermediate values. Conversely, not stripped galaxies are found at high values of X-ray emission.

In order to better quantify the impact that the hot gas or the cluster total mass can have on galaxy properties, we have investigated the distribution of morphologies and $H\alpha$ morphologies as a function of both X-ray emission and surface mass density distribution (plots not shown). While at low values of X-ray counts and surface mass density galaxies of all morphological types exist, only ellipticals are found at high values of surface mass density, and ellipticals and spirals at large X-ray count values. Focusing on $H\alpha$ properties, galaxies with a regular $H\alpha$ disk seem not to avoid very dense regions, where also asymmetric and clumpy objects are found.

It would be interesting to investigate the hot gas and surface mass density ranges over which the different physical processes take place, but given the small size of our sample, significant trends can not be detected.

To conclude, even though some trends are only tentative, cluster properties like the hot gas density or the dark matter distribution seem to have an impact on the $H\alpha$ morphology, and thus on the location of ongoing star formation, only in unrelaxed clusters. The lack of strong correlations does not allow us to identify a unique strong environmental effect that originates from the cluster center.

In the next section we will investigate whether some local effects, uncorrelated to the cluster-centric radius, play a larger role.

4.3. $H\alpha$ morphologies as a function of the projected local galaxy density

Figure 7 correlates the 2D distance between the peak of the $H\alpha$ emission and that of the continuum, as traced by the

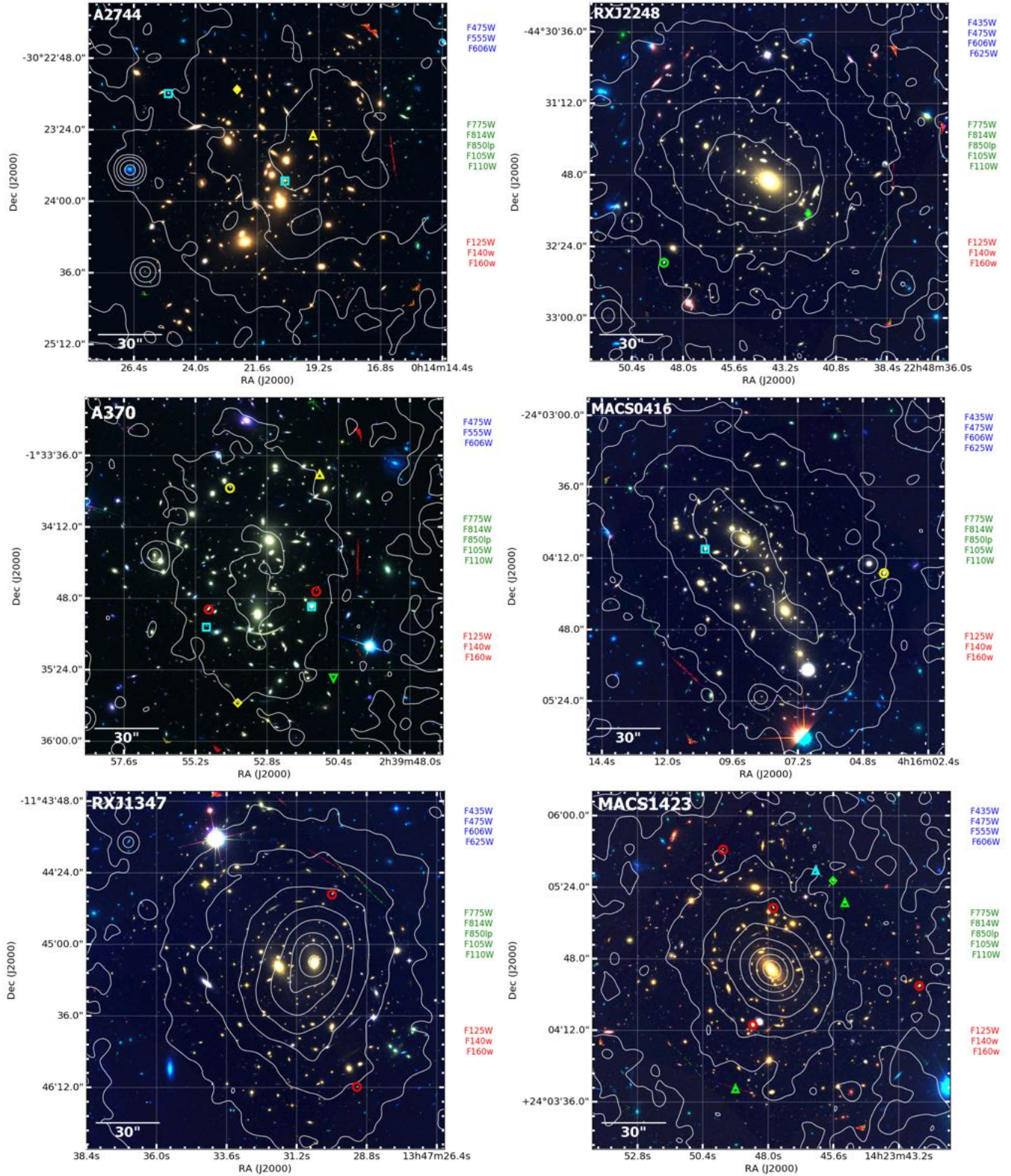


FIG. 4.— Color composite image of the 10 GLASS clusters. Images are based on the CLASH (Postman *et al.* 2012) or HFF (Lotz *et al.* 2016) HST data. The blue, green, and red channels are composed by the filters on the right. X-ray count contours are overplotted. Contours are spaced on a log scale from 0 to 1 counts/s/kpc². H α emitters with different H α morphologies (different colors) and experiencing different processes (different symbols) are also highlighted. Red symbols: regular H α , green symbols: clumpy H α , yellow symbols: concentrated H α , cyan symbols: asymmetric H α . Circles: regular process, squares: ram-pressure stripping, triangles: major-mergers, diamonds: minor mergers, inverted triangles: other.

F475W, to the projected local galaxy density. More precisely, it considers the absolute value of the offsets (not projected along the clustercentric distance) in the two directions (ob-

tained from the two different PAs) and, for the galaxies with both PAs, the real distance between the two peaks, obtained by combining the offsets.

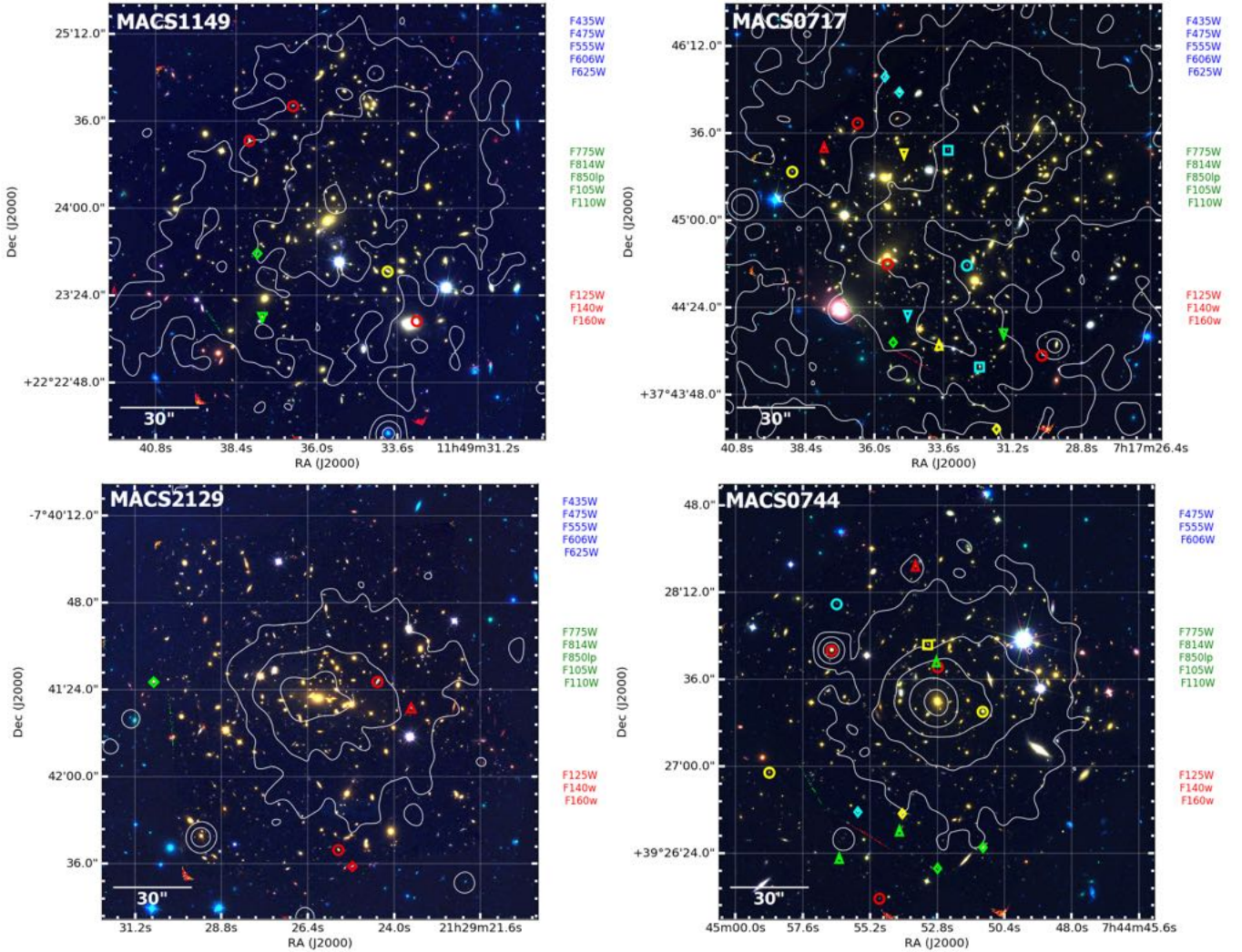


FIG. 4 (CONTINUES).—

The magnitude of the offset does not seem to correlate with the local density (Spearman correlation tests are always inconclusive), even though there might be an excess at intermediate values of local density. Nonetheless, some segregation effects between local density and $H\alpha$ properties (different colors in Figure 7) are visible.

Galaxies with concentrated $H\alpha$ seem to be preferentially found at lower densities, while galaxies with asymmetric $H\alpha$ seem to prefer denser environments. Galaxies with regular and clumpy $H\alpha$ are found at intermediate values of local density. K-S tests confirm that each population is drawn from a different parent distribution with high significance levels ($>90\%$), except for galaxies with regular and clumpy $H\alpha$.

Regular processes seem to operate at low to intermediate densities, as is also true for mergers. In contrast, ram-pressure stripping and unidentified processes tend to operate also at higher densities. A K-S test can reject the null hypothesis that a regular process and ram-pressure stripping are drawn from the same distribution at $\sim 90\%$ confidence.

To conclude, despite the statistics limited to 4 out of 10 GLASS clusters, trends with local densities are stronger than trends with the other tracers.

4.4. *sSFRs as a function of environment*

Understanding the origin of the trends of star formation with cluster properties represent a significant step forward toward comprehending the link between galaxy evolution and environment. If galaxy properties depend on the mass of the system where they reside or have resided during their evolution, there should be a connection between the trends observed and the way cosmological structures have grown in mass with redshift.

In Vulcani *et al.* (2010) and Paper VII we have found that the SFR-mass relation depends on environment: while many galaxies in clusters can be as star-forming as galaxies in the field, in the more massive systems a population of galaxies with a reduced SFR at fixed mass is detected. This result indicates that some cluster-specific processes that suppress star formation are taking place.

Here we just focus on clusters, and search for differences in the typical star forming properties for galaxies living in different conditions. To remove the influence of the stellar mass, we consider the Specific Star Formation Rate (sSFR), defined as the SFR per unit of galaxy stellar mass. As shown in Figure 8 the mean sSFR seems to depend on neither global nor local environment.

Considering separately galaxies with different $H\alpha$ morphology and/or experiencing different processes, no trends

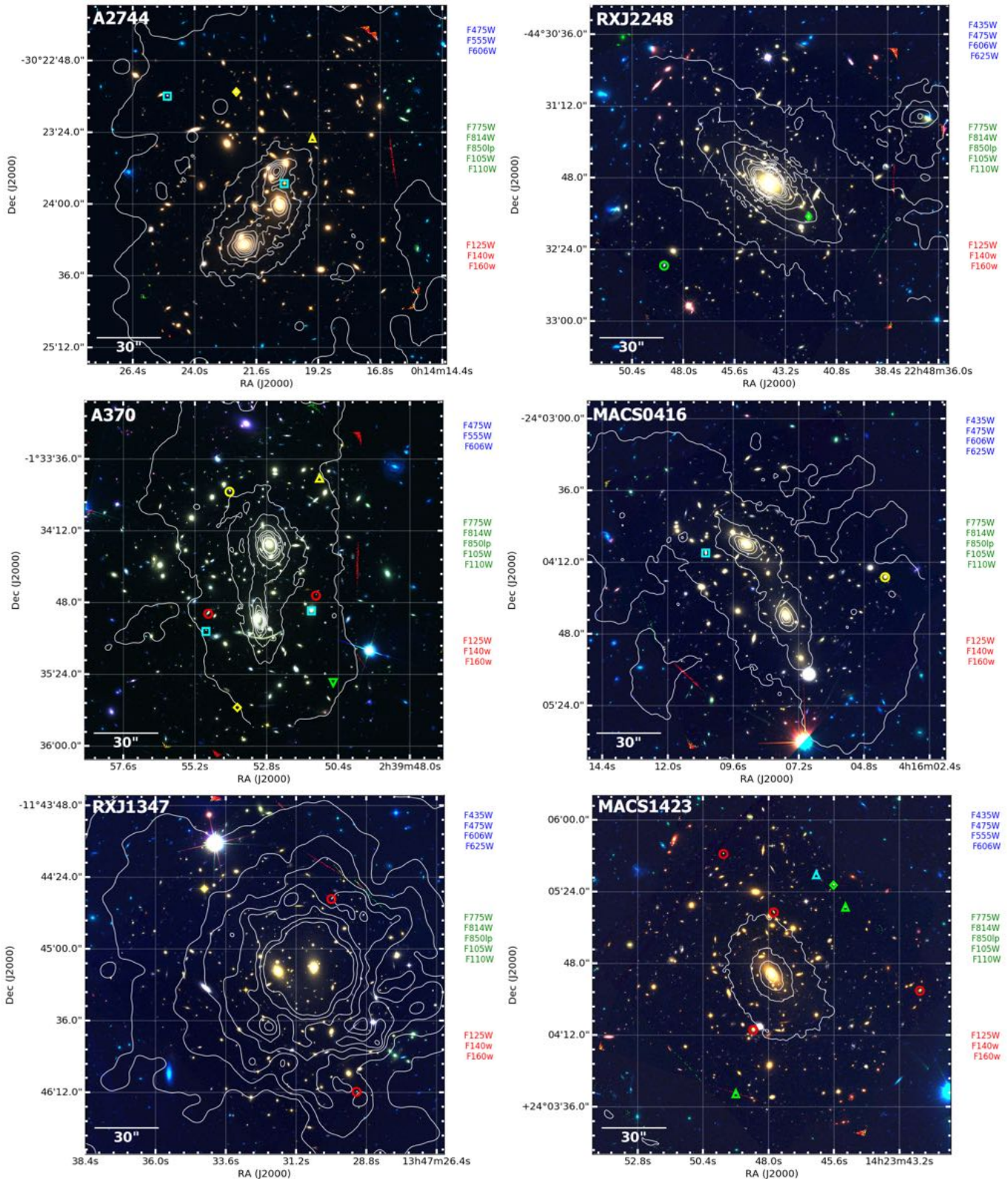


FIG. 5.— Color composite image of 9 GLASS clusters for which surface mass density maps are available. Images are based on the CLASH (Postman *et al.* 2012) or HFF (Lotz *et al.* 2016) HST data. The blue, green, and red channels are composed by the filters on the right. Surface mass density contours are overplotted. Contours are spaced on a linear scale in the range $10^{-5} - 10^{-3} \times 10^{12} M_{\odot} kpc^{-2}$. H α emitters with different H α morphologies (different colors) and experiencing different processes (different symbols) are also highlighted. Colors and symbols are as in Figure 4.

emerge.

Putting together these results and those presented in Vulcani *et al.* (2010) and Paper VII, we conclude that while differences emerge when comparing the most different environ-

ments in the Universe (clusters vs. field), the properties of the clusters do not seem to strongly influence the star formation in the cluster members. However, all these trends will need to be confirmed or refuted with larger number statistics.

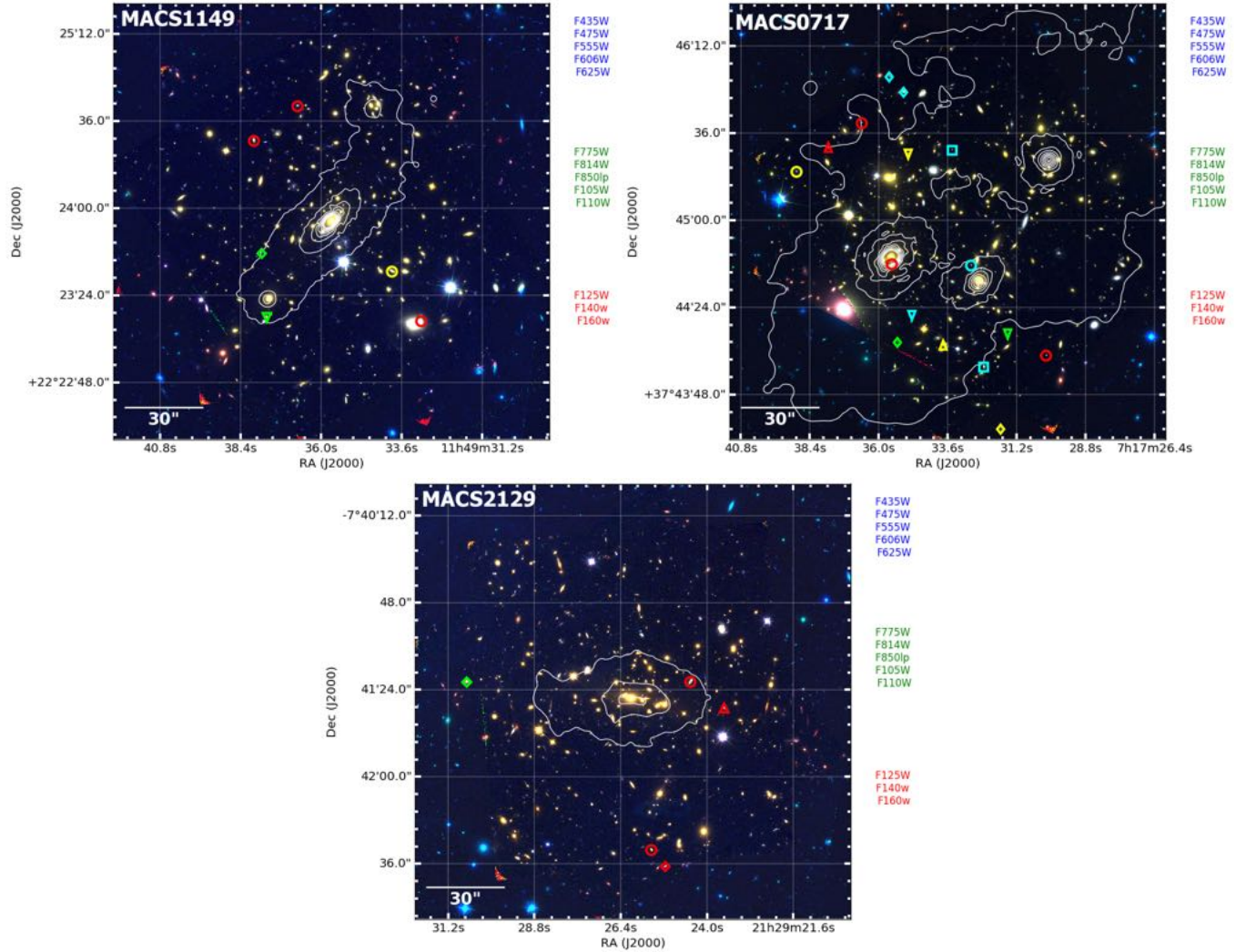


FIG. 5 (CONTINUES).—

We stress that we do not have all measurements for all our clusters, so our sample could be affected by incompleteness. Indeed, in principle, results from the clusters not included in our sample could differ from those presented here. Nonetheless, our findings are based on a random subset of the whole sample, therefore, for each measurement, the incompleteness is not related to cluster properties, so we do not expect strong biases.

We also note that our lack of trends is most likely due to the fact that, as discussed in Paper VII, our sample has been assembled by selecting visually detected $H\alpha$ emitters and therefore includes only highly star forming objects which most likely are at the first infall. Their SFR might therefore not been yet affected by the dense cluster environment. To properly characterize the effect of the environment one should focus on galaxies that have been part of the system for a long time and reaching lower SFR levels.

4.4.1. Comparison with previous work

Many authors have investigated the relation between star formation in galaxies as a function of environment, mainly focusing on the star forming fractions (e.g., Poggianti *et al.* 2006; Dressler *et al.* 2013; Zabludoff & Mulchaey 1998; Biviano *et al.* 1997; Smail *et al.* 1998). For our sample it is not straightforward to perform a similar analysis, since the

GLASS dataset does not yield redshifts for passive galaxies. Nonetheless, the fact that we do not find trends with the environment is overall in agreement with previous analyses.

Overall, at intermediate redshifts ($z \sim 1$), there is still no consistencies between different works: while some studies show a lower SFR or sSFR in denser regions compared to less-dense ones (e.g., Patel *et al.* 2009; Muzzin *et al.* 2012), some provide evidence for flat relations (e.g., Grützbauch *et al.* 2011; Scoville *et al.* 2013), and there are even reports of a correlation between star formation activity and density (e.g., Elbaz *et al.* 2007; Cooper *et al.* 2008; Welikala *et al.* 2016).

Finn *et al.* (2005), investigating 3 clusters at $z \sim 0.75$, found that the fraction of star-forming galaxies increases with projected distance from the cluster center and decreases with increasing local galaxy surface density, but the average SFR does not (see also Dressler 1980; Dressler *et al.* 2016). Comparing galaxies in clusters at $z \sim 0$ and $z \sim 0.5$, Poggianti *et al.* (2008) found that in both nearby and distant clusters, higher density regions contain proportionally fewer star-forming galaxies, and the average [OII] equivalent width of star-forming galaxies is independent of local density. Their results suggest that at high z the current star formation activity in star-forming galaxies does not depend strongly on global or local environment.

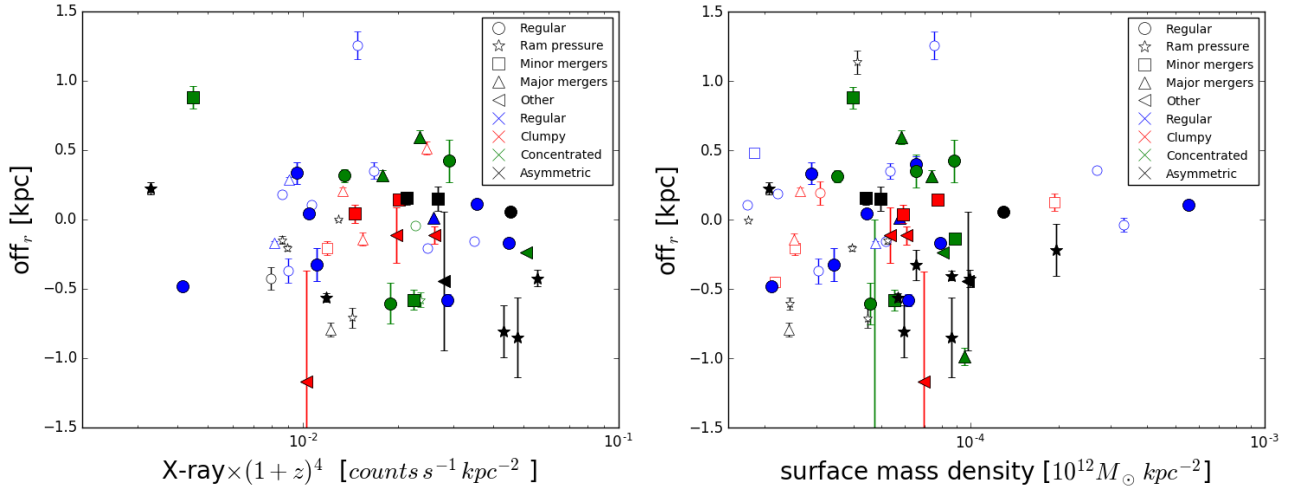


FIG. 6.— Correlation between the radial projected offset and the X-ray emission (left) and surface mass density (right) for galaxies with different $H\alpha$ morphology (color) and experiencing different physical processes (symbols), as indicated in the label. Filled symbols represent galaxies in unrelaxed clusters, empty symbols galaxies in relaxed clusters. The radial offset does not correlate with either the X-ray emission or the surface mass density distribution when the whole sample is considered, but it anti-correlates for merging systems.

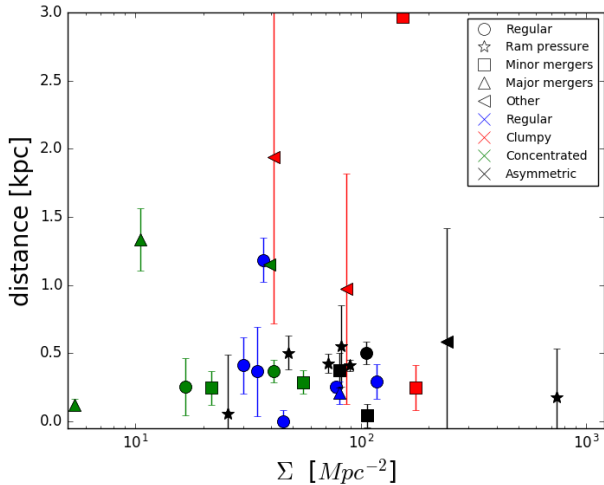


FIG. 7.— Correlation between the 2D distance between the $H\alpha$ emission and the continuum emission (F475W filter) and the projected local number density, for galaxies with both PAs. Galaxies with different $H\alpha$ morphology and experiencing different physical processes are shown using different color and symbols, as indicated in the label. The magnitude of the offset does not seem to correlate with the local density, even though there might be an excess at intermediate values of local density.

Similarly, at $z < 0.1$, Balogh *et al.* (2004) found that the relative numbers of star-forming and quiescent galaxies varies strongly and continuously with local density (see also Kauffmann *et al.* 2004; Baldry *et al.* 2006; Darvish *et al.* 2016). However, amongst the star-forming population, the distribution of the equivalent width of $H\alpha$, which can be used as a proxy for the strength of the specific star formation, is independent of environment (see also Tanaka *et al.* 2004; Wijesinghe *et al.* 2012). In contrast, von der Linden *et al.* (2010) found a marked anticorrelation between star formation and radius, which is most pronounced for low-mass galaxies and is very weak or absent beyond the virial radius. Discrepancies among the different studies can be explained in terms of the different SFR completeness limits reached: in von der Linden *et al.* (2010) the decline in SFR is driven largely by the inclusion of green galaxies into the sample of star-forming galaxies with low levels of star formation, which are instead missing in Balogh *et al.* (2004) and Tanaka *et al.* (2004) samples.

5. SUMMARY AND CONCLUSIONS

Building on our previous work described in Paper V and Paper VII, we have carried out a detailed investigation of the spatial distribution of star formation in galaxies at $0.3 < z < 0.7$, as traced by the $H\alpha$ emission in the 10 GLASS clusters.

$H\alpha$ maps were produced taking advantage of the WFC3-G102 data at two orthogonal PAs. We have visually selected galaxies with $H\alpha$ in emission and, based on their redshift, assigned their membership to the cluster. Following Paper VII, we have computed SFRs, and visually classified galaxies, paying particular attention to their broad-band morphology, and their $H\alpha$ morphology. The new scheme introduced in Paper VII visually categorizes galaxies according to the main process that is affecting the mode of star formation. Ours is clearly a qualitative and approximate classification scheme, considering that multiple processes might be simultaneously at work, but we believe there is merit in categorizing in a self consistent manner the diversity of morphological features across environments.

In this paper we have correlated the $H\alpha$ morphology with environmental conditions in which galaxies are embedded, focusing on the clustercentric distance, the hot gas density from X-ray emission, the total surface mass density from gravitational lensing and the local projected number density, to give a better insight on the role of the cluster environment in driving galaxy transformations.

Our main results can be summarized as follows.

- $H\alpha$ emitters can be found both close to the cluster center and up to $0.5r_{500}$, which is the maximum radius covered by GLASS. The radial projected offset between the peak of the $H\alpha$ emission and the peak in the continuum (as traced by the F475W filter) is negative for 60% of $H\alpha$ emitters, indicating that for most of them ionized gas is preferentially displaced away from the cluster center. In contrast, the distribution of the tangential offset shows no preferential direction. This result is solid at $\sim 2\sigma$ level.
- In order to quantitatively test the hypothesis that ram-pressure stripping is the main driver of the observed radial offsets between $H\alpha$ and the continuum, we compare with the Jiang *et al.* (2015) numerical simula-

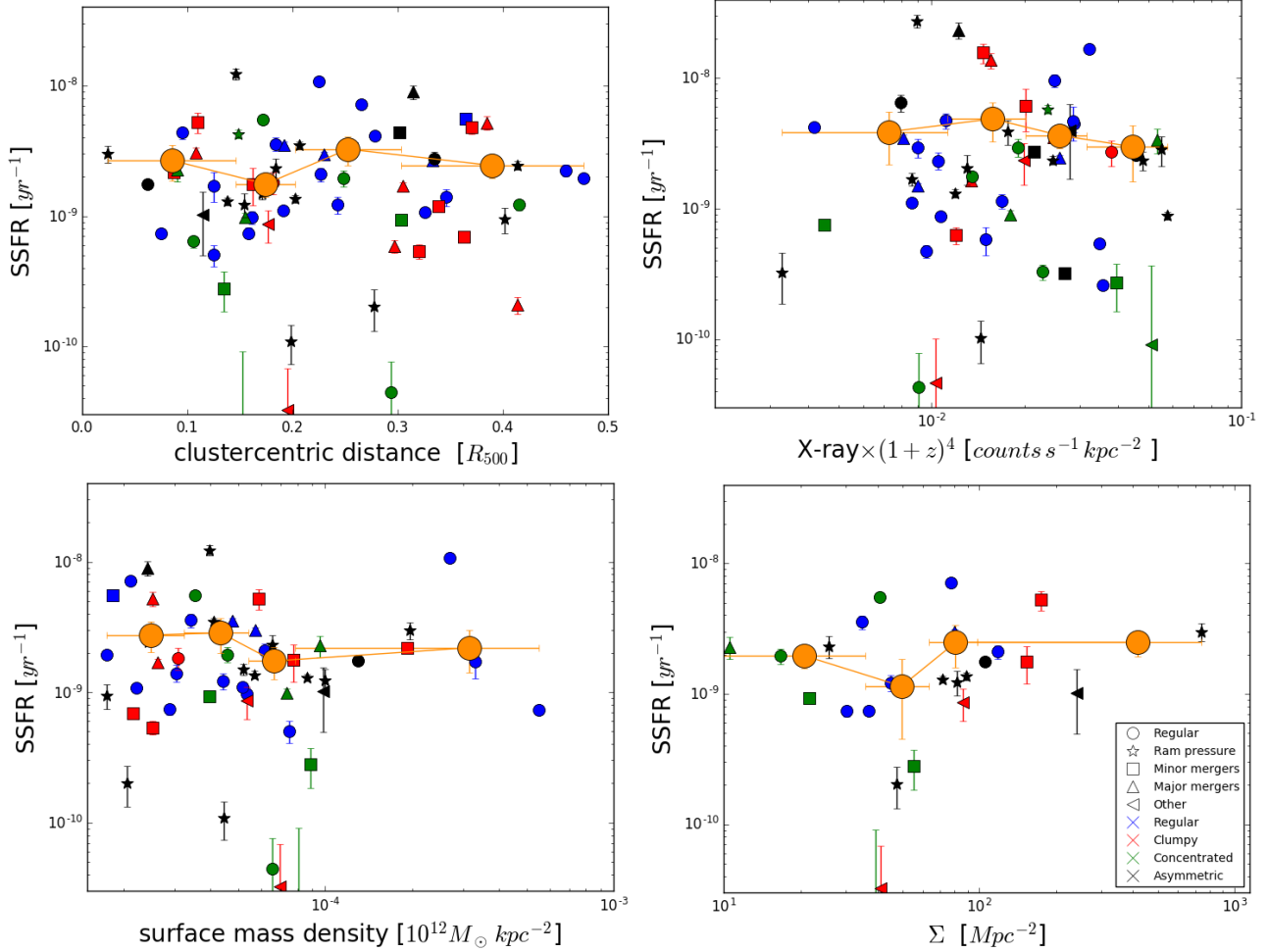


FIG. 8.— sSFR as a function of different parameterizations of environment for galaxies with different H α morphology and experiencing different physical processes, as indicated in the label. Errors on the individual measurements are typically smaller than the symbols. Big orange dots with errorbars indicate mean values in four equally-populated bins of the considered quantity. Upper left panel: clustercentric distance (all clusters), upper right panel: X-ray counts (all clusters), bottom left panel: surface mass density values (nine clusters), bottom right panel: projected local density (four clusters). All trends appear flat, indicating that the average sSFR in star forming galaxies does not depend on either global or local environment.

tions. As expected, given the small clustercentric radius of observation of the H α emitters, they consist of the 25% most radial orbits found in cosmological simulations. Assuming that the direction of the offset between H α and continuum can be taken as proxy for the direction of motion at the time of observations, we find that the observed distribution of directions is consistent with the expectations for infalling galaxies in cosmological simulations. The agreement improves when we consider only galaxies visually classified as undergoing ram-pressure stripping, providing quantitative support for our interpretation of the morphology.

- Our clusters cover a wide range of morphologies: some of them are relaxed, while others are merging systems presenting very asymmetric configurations, as probed by the different surface mass density distributions and X-ray emissions. Galaxies characterized by all kinds of H α morphologies and experiencing the different processes can be found in almost all clusters and significant trends cannot be detected using this relatively small data sample. However, when considering only unrelaxed clusters we find that galaxies found in correspondence of a peak in the X-ray and surface mass distributions have more negative offsets. This indicates that

a mechanism related to an interaction with these ICM features may be in some cases responsible for an alteration in the star forming properties.

- Whereas the amplitude of the offset between the peak of the H α emission and the peak in the continuum (as traced by the F475W filter) does not depend on local density, we recovered some hints that H α morphologies do. Galaxies with concentrated H α seems to be preferentially found at lower densities, while galaxies with asymmetric H α might prefer denser environments. Galaxies with regular and clumpy H α are found at intermediate values of local density. K-S tests support these findings. In addition, as expected, mergers are found at low to intermediate densities. In contrast, ram-pressure stripping and unclassified processes tend to operate at higher densities.
- The most statistically significant result is that galaxies with asymmetric H α distribution, interpreted as signatures of recent ram pressure stripping, are preferentially found within $0.3 r_{500}$, at higher local density conditions and higher X-ray counts and have a negative radial projected offset, i.e. the peak of the H α emission is pointing away from the cluster center with respect to the con-

tinuum emission.

- Overall, the average sSFR in star forming galaxies does depend on neither global nor local environment. These findings will have to be confirmed or refuted by larger number statistic, but, if true, they suggest that the properties of the clusters are not able to strongly affect the star formation in clusters. However, it is important to stress that our sample includes only highly star forming objects which most likely are at the first infall. Their SFR might therefore not been yet affected by the dense cluster environment. To properly characterize the effect of the environment one should focus on galaxies that have been part of the system for a long time. Galaxies with concentrated H α are preferentially found at lower densities, while galaxies with asymmetric H α prefer denser environments. Galaxies with regular and clumpy H α are found at intermediate values of local density. K-S tests confirm that each population is drawn from a different parent distribution with high significance levels (>90%), except for galaxies with regular and clumpy H α .

Based on these observations, we conclude that in clusters the population of star-forming galaxies, as traced by the H α emission, is very heterogeneous. Although living in the most extreme environments of the Universe, a considerable fraction of galaxies still are not affected by the surrounding conditions and present regular H α morphologies not affected by any strong physical process. Nonetheless, many galaxies respond to the extreme conditions in which they are embedded, especially those in unrelaxed clusters. They show torqued, asymmetric, clumpy H α morphologies. Many different processes are thought to be responsible for these observations and no unique physical process emerges as dominant. Overall, the most evident trends have been detected with the local density, suggesting that local effects play a larger role than those correlated to the clustercentric radius. Such effects weaken potential radial trends.

Following Dressler (1980), in the past several years significant evidence has been accumulated that several of the main galaxy properties, such as the galaxy mass, the red galaxy population, and the morphological types of galaxies, are better correlated with the local environment than the global en-

vironment. Both at $z \sim 0.6$ and $z \sim 0$, Vulcani *et al.* (2012) found that the shape of the galaxy stellar mass function depends on local density, while variations with the global environment (intended as cluster vs. field) are very subtle (Vulcani *et al.* 2013; Calvi *et al.* 2013). In local clusters, none of the characteristics of the colour-magnitude red sequence (slope, scatter, luminous-to-faint ratio, blue fraction and morphological mix on the red sequence) depends on global cluster properties connected with cluster mass, such as cluster velocity dispersion and X-ray luminosity. In contrast, all of these characteristics vary systematically with the local galaxy density (Valentinuzzi *et al.* 2011). In addition, the fractions of spiral, S0 and elliptical galaxies do not vary systematically with cluster velocity dispersion and X-ray luminosity (Poggianti *et al.* 2009), while a strong morphology-density relation is present (Fasano *et al.* 2015). Moreover, Balogh *et al.* (2004) found that the red fraction of galaxies is a strong function of local density, increasing from $\sim 10 - 30\%$ of the population in the lowest density environments to $\sim 70\%$ at the highest densities, while within the virialized regions of clusters it shows no significant dependence on cluster velocity dispersion. Also, Martínez, Coenda & Muriel (2008) found that bright galaxy properties do not clearly depend on cluster mass for clusters more massive than $M_* \sim 10^{14} M_\odot$, while they correlate with cluster-centric distance.

All these studies suggest that local processes, such as ram pressure, strangulation and galaxy-galaxy interactions are the most easily detectable drivers of environmental evolution. However, they must work simultaneously with processes taking place on large scale, such as cluster-galaxy interactions, which apparently just leave more subtle signs.

ACKNOWLEDGMENTS

We thank the referee for their comments, which helped us to improve the manuscript. Support for GLASS (HST-GO-13459) was provided by NASA through a grant from the Space Telescope Science Institute, which is operated by the Association of Universities for Research in Astronomy, Inc., under NASA contract NAS 5-26555. We are very grateful to the staff of the Space Telescope for their assistance in planning, scheduling and executing the observations. B.V. acknowledges the support from an Australian Research Council Discovery Early Career Researcher Award (PD0028506).

REFERENCES

- Abramson, L. E. *et al.* 2016, ArXiv e-prints.
 Baldry, I. K. *et al.* 2006, MNRAS, 373, 469.
 Balogh, M. L. *et al.* 2004, ApJ, 615, L101.
 Balogh, M. L., Navarro, J. F., and Morris, S. L. 2000, ApJ, 540, 113.
 Bekki, K. 1999, ApJ, 510, L15.
 Bekki, K. and Couch, W. J. 2003, ApJ, 596, L13.
 Bekki, K., Owers, M. S., and Couch, W. J. 2010, ApJ, 718, L27.
 Berrier, J. C. *et al.* 2009, ApJ, 690, 1292.
 Biviano, A. *et al.* 1997, A&A, 321, 84.
 Bradač, M. *et al.* 2005, A&A, 437, 39.
 Bradač, M. *et al.* 2009, ApJ, 706, 1201.
 Brammer, G. B. *et al.* 2012, The Astrophysical Journal Supplement, 200, 13.
 Butcher, H. and Oemler, Jr., A. 1984, ApJ, 285, 426.
 Calvi, R. *et al.* 2013, MNRAS, 432, 3141.
 Capak, P. *et al.* 2007, ApJS, 172, 284.
 Chabrier, G. 2003, PASP, 115, 763.
 Cooper, M. C. *et al.* 2008, MNRAS, 383, 1058.
 Cowie, L. L. and Songaila, A. 1977, Nature, 266, 501.
 Crane, P. and Saslaw, W. C. 1986, ApJ, 301, 1.
 Darvish, B. *et al.* 2016, ApJ, 825, 113.
 De Lucia, G. and Borgani, S. 2012, MNRAS, 426, L61.
 Dressler, A. 1980, ApJ, 236, 351.
 Dressler, A. *et al.* 2016, ArXiv e-prints.
 Dressler, A. *et al.* 1997, ApJ, 490, 577.
 Dressler, A. *et al.* 2013, ApJ, 770, 62.
 Ehlert, S. *et al.* 2013, MNRAS, 428, 3509.
 Elbaz, D. *et al.* 2007, A&A, 468, 33.
 Ellis, R. S. *et al.* 1997, ApJ, 483, 582.
 Fasano, G. *et al.* 2015, MNRAS, 449, 3927.
 Fasano, G. *et al.* 2000, ApJ, 542, 673.
 Finn, R. A. *et al.* 2005, ApJ, 630, 206.
 Fujita, Y. *et al.* 1999, PASJ, 51, L1.
 Garn, T. and Best, P. N. 2010, MNRAS, 409, 421.
 Gómez, P. L. *et al.* 2003, ApJ, 584, 210.
 Goto, T. *et al.* 2003, MNRAS, 346, 601.
 Grützbauch, R. *et al.* 2011, MNRAS, 412, 2361.
 Gunn, J. E. and Gott, III, J. R. 1972, ApJ, 176, 1.
 James, P. A. *et al.* 2005, A&A, 429, 851.
 Jiang, L. *et al.* 2015, MNRAS, 448, 1674.
 Kauffmann, G. *et al.* 2004, MNRAS, 353, 713.
 Kennicutt, R. C., Tamblyn, P., and Congdon, C. E. 1994, Astrophysical Journal, 435, 22.
 Kriek, M. *et al.* 2009, ApJ, 700, 221.
 Larson, R. B., Tinsley, B. M., and Caldwell, C. N. 1980, ApJ, 237, 692.

- Lewis, I. *et al.* 2002, MNRAS, 334, 673.
Lilly, S. J. and Carollo, C. M. 2016, ArXiv e-prints.
Londrillo, P., Nipoti, C., and Ciotti, L. 2003, Memorie della Societa Astronomica Italiana Supplementi, 1, 18.
Lotz, J. M. *et al.* 2016, ArXiv e-prints.
Madau, P., Pozzetti, L., and Dickinson, M. 1998, ApJ, 498, 106.
Mantz, A. *et al.* 2010, MNRAS, 406, 1773.
Martínez, H. J., Coenda, V., and Muriel, H. 2008, MNRAS, 391, 585.
McGee, S. L. *et al.* 2009, MNRAS, 400, 937.
Momcheva, I. G. *et al.* 2015, ArXiv e-prints.
Moore, B. *et al.* 1996, Nature, 379, 613.
Morishita, T. *et al.* 2016, ArXiv e-prints.
Muzzin, A. *et al.* 2012, ApJ, 746, 188.
Navarro, J. F., Frenk, C. S., and White, S. D. M. 1996, ApJ, 462, 563.
Nipoti, C. 2017, MNRAS, in press (arXiv:1612.06420).
Nipoti, C., Londrillo, P., and Ciotti, L. 2003, MNRAS, 342, 501.
Nulsen, P. E. J. 1982, MNRAS, 198, 1007.
Oesch, P. A. *et al.* 2010, The Astrophysical Journal Letters, 709, L16.
Owers, M. S. *et al.* 2012, ApJ, 750, L23.
Paccagnella, A. *et al.* 2016, ApJ, 816, L25.
Patel, S. G. *et al.* 2009, ApJ, 705, L67.
Poggianti, B. M. *et al.* 2004, ApJ, 601, 197.
Poggianti, B. M. *et al.* 2008, ApJ, 684, 888.
Poggianti, B. M. *et al.* 2009, ApJ, 697, L137.
Poggianti, B. M. *et al.* 1999, ApJ, 518, 576.
Poggianti, B. M. *et al.* 2006, ApJ, 642, 188.
Postman, M. *et al.* 2012, ApJS, 199, 25.
Postman, M. *et al.* 2005, ApJ, 623, 721.
Schmidt, K. B. *et al.* 2014, ApJ, 782, L36.
Scoville, N. *et al.* 2013, ApJS, 206, 3.
Smail, I. *et al.* 1998, MNRAS, 293, 124.
Tanaka, M. *et al.* 2004, AJ, 128, 2677.
Treu, T. *et al.* 2003, ApJ, 591, 53.
Treu, T. *et al.* 2015, ApJ, 812, 114.
Valentinuzzi, T. *et al.* 2011, A&A, 536, A34.
Vijayaraghavan, R. and Ricker, P. M. 2013, MNRAS, 435, 2713.
von der Linden, A. *et al.* 2014, MNRAS, 439, 2.
von der Linden, A. *et al.* 2010, MNRAS, 404, 1231.
Vulcani, B. *et al.* 2011, MNRAS, 412, 246.
Vulcani, B. *et al.* 2012, MNRAS, 420, 1481.
Vulcani, B. *et al.* 2010, ApJ, 710, L1.
Vulcani, B. *et al.* 2013, A&A, 550, A58.
Vulcani, B. *et al.* 2016, ApJ, 833, 178.
Vulcani, B. *et al.* 2015, ApJ, 814, 161.
Welikala, N. *et al.* 2016, MNRAS, 455, 1629.
Wijesinghe, D. B. *et al.* 2012, MNRAS, 423, 3679.
Yagi, M. *et al.* 2015, AJ, 149, 36.
Zabludoff, A. I. and Mulchaey, J. S. 1998, ApJ, 496, 39.